Research Article



# Directed vascularization in bone regeneration requires bone marrow reconstitution

Julia Mehl<sup>1,2</sup>, Tobias Thiele<sup>1,2</sup>, Agnes Ellinghaus<sup>1,2</sup>, Holger Gerhardt<sup>3,4</sup>, Georg N. Duda<sup>1,2,\*</sup>

- <sup>1</sup>Julius Wolff Institute, Berlin Institute of Health at Charité Universitätsmedizin Berlin, Berlin 13353, Germany
- <sup>2</sup>Berlin Institute of Health Center for Regenerative Therapies, Berlin Institute of Health at Charité Universitätsmedizin Berlin, Berlin 13353, Germany
- 3 Max-Delbrück-Center for Molecular Medicine (MDC) in the Helmholtz Association, Berlin 13125, Germany
- <sup>4</sup>German Center for Cardiovascular Research (DZHK) Partnersite Berlin, Berlin 10785, Germany
- \*Corresponding author: Georg N. Duda, Julius Wolff Institute and Berlin Institute of Health Center for Regenerative Therapies, Berlin Institute of Health at Charité Universitätsmedizin Berlin, Augustenburger Pl. 1, Berlin 13353, Germany (georg.duda@charite.de).

#### **Abstract**

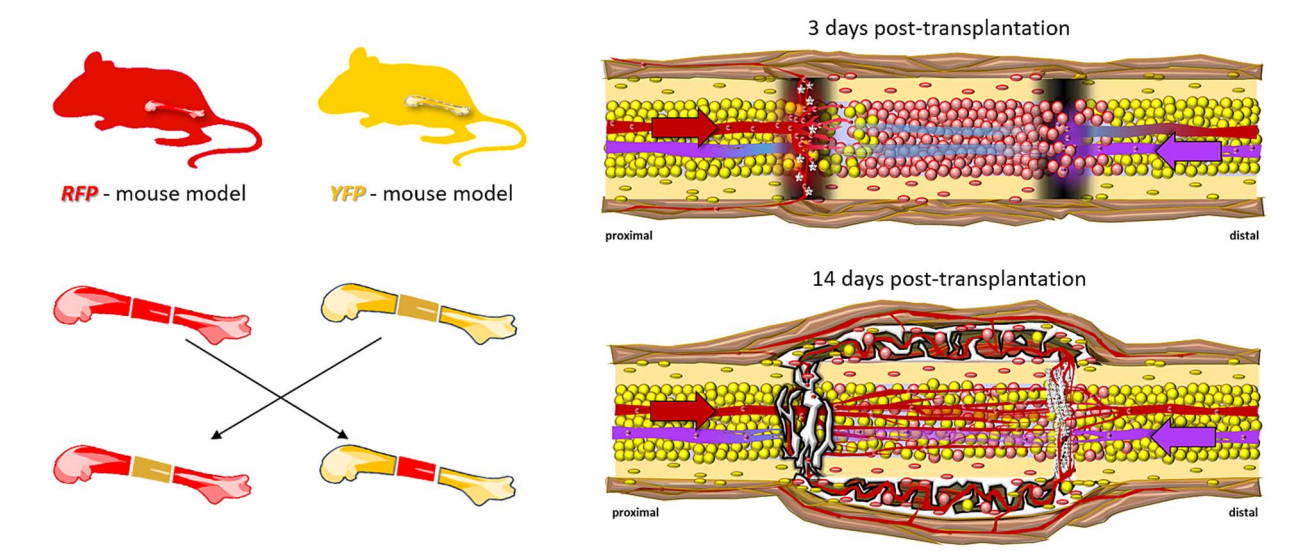
Bone has the unique ability to regenerate without scarring, yet the cellular dynamics and directional organization underlying this process, and how they are linked to marrow reconstitution, remain incompletely understood. To investigate these mechanisms, we developed a novel double osteotomy model in mice, involving transplantation of a 2-mm bone graft between genetically distinct fluorescent reporter lines (yellow fluorescent protein and red fluorescent protein). This approach enabled precise tracking of cellular migration and vascularization over 3, 7, and 14 d post-transplantation. Our findings revealed directed migration of host-derived proximal bone marrow cells into the graft, starting at day 3 and leading to complete host cell infiltration by day 14. CD146-positive blood vessels, mainly originating from the proximal host marrow, invaded the graft coinciding with graft marrow remodeling. Marrow disintegration within the graft occurred prior to vascular and cellular invasion, with subsequent reconstitution progressing from the proximal side. Flushing the graft marrow cavity prior to transplantation resulted in more extensive marrow niche formation by day 14 suggesting that marrow reconstitution can proceed more rapidly without the need for prior remodeling. This study introduces a new model to dissect the spatial and temporal coordination of cellular migration and vessel invasion during bone regeneration. Our results uncover the directional nature of healing and underscore the critical role of marrow reconstitution in guiding regenerative processes—insights that may inform surgical and biomaterial strategies to enhance bone repair.

Keywords: bone healing, bone graft transplantation, bone marrow reconstitution, directed healing, directed vascularization

#### Lav Summary

Successful bone healing requires not only the regrowth of bone but also the restoration of its marrow compartments including blood vessels. However, how these processes are coordinated in time and space remains poorly understood. Here, we studied healing using bone grafts and discovered that it is highly organized and directional, with graft bone marrow reorganization being tightly bound to blood vessel invasion. We show that orchestrated marrow reorganization is essential for cellular invasion and revascularization, with flushing the bone marrow promoting graft niche formation and enhancing bone formation.

## **Graphical Abstract**



## Introduction

Bone's unique ability to regenerate without scarring is driven by tightly coordinated series of cellular events triggered by injury, involving the infiltration of diverse cell types that reorganize the hematoma and blood clot.<sup>1-5</sup> An initial pro-inflammatory phase soon transitions to an anti-inflammatory phase, marked by rapid microvascular invasion that restores nutrient supply. Subsequently, cartilage and bone form through cellular differentiation processes, followed by cartilage-to-bone remodeling via endochondral ossification. Ongoing bone remodeling, mediated by a finely tuned balance between bone-forming osteoblasts and bone-resorbing osteoclasts, ultimately restores a fully loadbearing structure with mechanical strength and architecture comparable to the pre-injury bone.<sup>7</sup> Re-establishment of the bone cortex is accompanied by the reconstitution of the bone marrow cavity and the reorganization of its vascular network at the injury site. The restoration of a central marrow vasculature is a critical hallmark of effective bone regeneration.<sup>3</sup> Despite well-characterized healing cascades, the origin of cells that invade the injury site and initiate healing, as well as their spatiotemporal migration patterns during bone regeneration, remain poorly understood.

Among the invading cell populations, endothelial cells (ECs) that form vascular structures play a central role in regeneration. Revascularization of the injury region is essential not only for the early delivery of oxygen and nutrients but also for orchestrating later stages of tissue remodeling and bone marrow restoration. Invading blood vessels transport hematopoietic and stromal progenitor cells and secrete angiocrine signals that influence cell fate decisions in their local microenvironment, coordinate regeneration, and support the establishment of a functional bone marrow niche. Initial sprouting angiogenesis into the injured area is typically driven by VEGF gradients, which regulate the coordinated activity of tip and stalk ECs. 9-11 Beyond angiogenic cues, vascular network formation is also influenced by mechanical forces: EC migration relies on interactions with the extracellular matrix (ECM), including adhesion to ECM fibers that guide their movement, as well as hemodynamic forces generated by blood flow. 12,13 Despite

this understanding, the origin, organization, directionality, and temporal progression of angiogenic sprouting during bone healing remain poorly defined. Moreover, how the spatial and temporal patterns of vascular invasion during healing align with bone marrow reconstitution remain unknown.

Cell-ECM interactions that facilitate cell migration are partly mediated by cell adhesion molecules (CAMs), a class of surface proteins that regulate cell attachment.<sup>14</sup> One such molecule is cluster of differentiation 146 (CD146), also known as melanoma cell adhesion molecule (MCAM) or Muc18, a key marker of ECs.<sup>15</sup> CD146 also marks a perivascular cell population that helps maintain the vascular niche.<sup>16–19</sup> As a marker for both ECs and perivascular cells (pericytes), CD146 serves as an indicator of vascular integrity, making it optimal for tracking the complete vascular architecture along with its associated pericytes.

To better understand the chronological sequence and interplay between cellular migration and revascularization—and how these processes guide regeneration and are linked to bone marrow reconstitution during bone healing—we here present a novel strategy for analyzing these processes and their directionality. We developed a double osteotomy model in which a critical-size defect in one mouse is grafted with bone from a second, genetically distinct fluorescent reporter line—either red fluorescent protein (RFP) or yellow fluorescent protein (YFP). This dual-labeling approach enables precise tracking of host cell origin and migration into the graft, while also visualizing microvascular invasion via CD146, thereby allowing assessment of how cellular infiltration and vascular progression facilitate bone graft integration and marrow niche regeneration.

## Materials and methods Double mouse osteotomy model

Female mice with a C57BL/6J background expressing either ubiquitous RFP or YFP were used as donor and recipient, respectively. RFP and YFP are expressed in all somatic cells. The YFP and RFP mice were bred at the DRFZ (German Rheumatism Research Centre Berlin). For the transplantation

of the bone pieces, the 10-wk-old female mice were anesthetized with general anesthesia. After that, the anesthesia is maintained via a breathing mask with a 2% iso-flurane oxygen mixture. The mice receive a subcutaneous injection of 0.1 mg/kg Temgesic (buprenorphine) for complete analgesia and an injection of 45 mg/kg clindamycin to prevent infection. To prevent drying out of the eyes, they were protected with Bepanthen eye ointment. After checking for sufficient depth of anesthesia (interdigital reflex), a small skin incision is made laterally from the knee to the hip. From there, a blunt dissection is made through the fascia lata between the gluteus suprefialis and biceps femoris muscles to the femur. RFPlabeled 2 mm pieces of the bone shaft were cut with a wire saw (RISystem Gigli wire saw 0.22 mm RIS.590.100, Switzerland) and a custom-designed surgical guide (Charité, Technische Werkstätten, Berlin, Germany). This bone graft was then transplanted into a YFP mice, where a 2 mm bone defect was set previously. A distraction system was used to stabilize both the osteotomies and the bone graft (RISystem Distraction-MouseDis RIS.631.100, RISystem MouseExFix MountingPin 0.4 mm RIS.411.100, Switzerland). The wound was then sutured, and the animals were allowed to remain in their cage for the healing period. Intraoperative and postoperative exemplary images of the surgical procedure are provided in Figure S1. The drinking water of the mice is supplemented with tramadol hydrochloride (25 mg/L) for postoperative analgesia for 3 d. To ensure that the animals quickly resume eating after surgery, food is also provided on the cage floor. Mice were sacrificed by cervical dislocation 3, 7, and 14 d after transplantation. In one group the bone marrow was flushed out (0.9% NaCl) directly before transplantation. The animal experiment was approved by LAGeSo (LAGeSo, Berlin, Germany; G0289/15).

#### Bone preparation and cryocutting

After euthanasia, the femurs were harvested, taking special care to preserve the surrounding muscle tissue and to maintain the healing bone graft in place to enable precise spatial tracking of cell migration into the graft but also into the adjacent tissues. Bones were then fixed in 4% paraformaldehyde (PFA), decalcified in 0.5 M EDTA, prepared for freezing in a sucrose-PVP mixture and then embedded in a sucrose-PVP-gelatin mixture and finally frozen. For subsequent cryocutting, cryoblocks were secured to the cryotome sample holder using Tissue-Tek O.C.T. Compound (Sakura, #4583). About 50  $\mu$ m thick sections were then cut and immediately transferred to glass slides for immunofluorescence staining. In addition, 7  $\mu$ m thick sections were cut and then transferred to Kawamoto foil and then transferred to glass slides for Movat's pentachrome staining.

#### Immunofluoresence staining

About 50  $\mu$ m thick tissue cryosections were thawed and dried for 30 min at room temperature, followed by rehydration with ice-cold PBS for 5 min. Samples were then permeabilized with ice-cold 0.3% triton in water for 10 min which was subsequently followed by blocking with 5% normal serum donkey and 0.3% triton in 1xPBS for 30 min. Primary antibodies CD146 (CD146 MCAM, Abcam, ab75769, 1:200), CD31/PECAM-1 (R&D systems, #AF3628, 1:200), Endomucin (Santa Cruz, Cat# sc-65 495, 1:100), and Osterix/Sp7 (Abcam, ab22552, 1:200) were diluted in 5% normal serum donkey in PBS and incubated overnight at 4 °C. Samples were

then washed with ice-cold PBS for 5 min 3 times. Secondary antibodies were diluted in PBS with a 1:200 dilution. Some samples were additionally stained for nuclei using SYTOX blue (Invitrogen S11348). Samples were incubated with secondary antibody solution for 3 h before washing with PBS was performed. Samples were finally mounted with Fluoromount G (#Cat 0100-01, Southern Biotech).

## Movat's pentachrome staining

For Movat's pentachrome staining tissue sections were airdried for 30 min at room temperature and subsequently fixed in 4% formaldehyde solution for 10 min. After rinsing in distilled water for 5 min, sections were pretreated in 3% acetic acid, followed by incubation in 1% Alcian blue prepared in 3% acetic acid for 30 min. The sections were then rinsed in 3% acetic acid for 3 min, followed by rinsing in distilled water. Subsequently, they were incubated in alkaline ethanol for 1 h and subsequently put in water for 10 min. Sections were then stained in Weigert's iron hematoxylin solution for 15 min, again put in water for 10 min, followed by incubation in Brilliant-Crocein-Acid-Fuchsin solution for 15 min. After rinsing in 0.5% acetic acid, the sections were dehydrated in 100% ethanol (3 changes, 2 min each) and subsequently incubated in Safran du Gatinais for 1 h. This was followed by another dehydration step in 100% ethanol (3 changes, 2 min each) and clearing in xylene (2 changes, 2 min each). Finally, the Kawamoto tape was carefully removed from the original slide, transferred to a new slide, and mounted with Vitroclud.

## Imaging of stained tissue sections

Images of stained tissue sections, prepared with either Movat's pentachrome or immunofluorescence, were acquired using a Leica DM6 B Thunder Imager, capable of both brightfield and fluorescence microscopy. For thicker immunofluorescence-stained sections, z-stacks were captured. Additionally, fibrillar collagen in selected thicker immunofluorescence-stained cryosections was visualized by second harmonic generation (SHG) using a Leica SP5 confocal microscope equipped with a multiphoton laser. An excitation wavelength of 910 nm was used for SHG imaging.

## Histomorphometric analysis

Tissue composition was assessed from Movat's pentachrome stained sections by quantitatively analyzing newly formed bone, fibrous tissue, and bone marrow. Vascular invasion was evaluated and quantified from CD146 immunofluorescence images. All histomorphometric analyses were performed in Fiji using custom-designed macros. In the first macro, ROIs were defined to encompass the entire transplanted area, including the proximal host bone, the graft, the distal host bone, and both graft-host interfaces. For quantification of tissue composition and vascular/cellular ingrowth, the bone axis was divided into 8 equal-sized zones, each 250  $\mu$ m in length. This segmentation produced a total of 26 sections spanning the proximal-to-distal axis, enabling region-specific analysis across all samples and time points. This approach also enabled graphical visualization of the data for each ROI, providing a clear spatial representation of changes in tissue composition and vascularization along the bone axis, and allowing direct comparison between regions. The second macro was used to classify tissue types within each ROI. Classification combined manual annotation with color segmentation in the HSB color model, based on Movat's

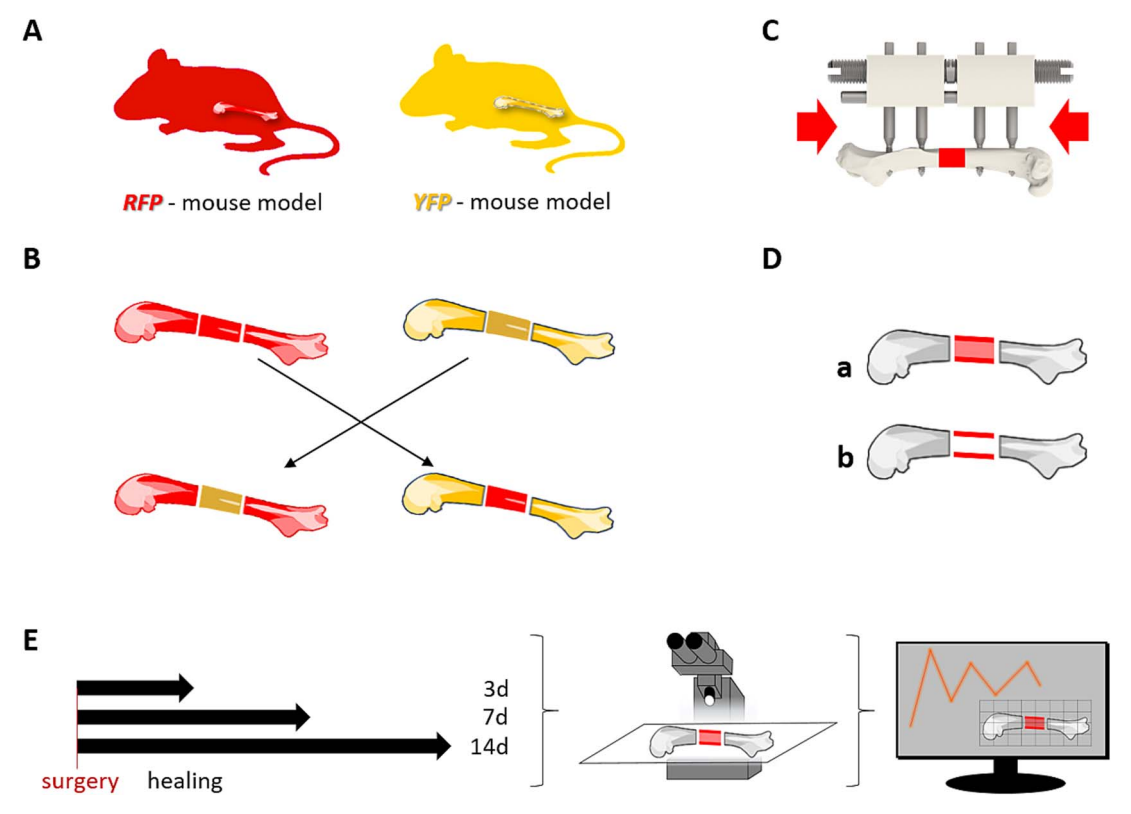


**Figure 1.** Experimental design of the transplant model to track cellular migration and vascularization. (A) Mice expressing either the ubiquitous red fluorescent protein (RFP) or the yellow fluorescent protein (YFP) on a B6 background were used. (B) Schematic representation of the model enabling transplantation of RFP bone graft into YFP bone or vice versa. (C) Distraction system was applied to stabilize the grafted bone and hold it in place. (D) The analysis included groups in which the entire bone graft segment was transplanted (+bone marrow) (a) and a group in which the bone marrow was flushed out from the bone graft (-bone marrow) (b). (E) The mice were sacrificed 3, 7, and 14 d after transplantation. The tissue samples were then analyzed by histological methods, followed by microscopic imaging.

pentachrome stained images. Additionally, custom-developed scripts integrated with Fiji were used to: Measure vessel area within each ROI, determine vessel orientation and generate heatmap-based quantifications of vascular network density. Nuclear density was assessed from SYTOX-stained sections by measuring fluorescence intensity along the proximal-to-distal axis within the defined ROIs.

#### **Statistics**

Statistical analyses were conducted using Microsoft SPSS (Version 28.0.0.0 (190), IBM, Armonk, NY, USA). Mann-Whitney U test was used to assess statistical significance between two groups, since the data were not normally distributed. For comparisons between three groups, the Kruskal–Wallis test was applied, followed by Dunn's multiple comparisons post-hoc test. A *p*-value <.05 was considered statistically significant. Exact *p*-values and sample size for each analysis ("n") are indicated in the corresponding figures.

#### Results

## At early time points, bone marrow-derived host cells invaded the graft from the proximal side

Mice expressing either ubiquitous YFP or RFP were used in the study. A 2 mm piece from the midshaft of the femur of the RFP-expressing mice was transplanted into the femur of the YFP-expressing mice. Consequently, red and yellow fluorescence cells represented transplanted graft and host cells, respectively. This allowed the tracking of cellular origins within the integrated tissue. Following the transplantation of the bone graft into the host bone, we analyzed the integration of the graft into the host bone (Figure 1A-C). To assess the very early stages of this integration, mice were sacrificed after a 3-d healing period (Figure 1E). At 3 d post-transplantation, specific areas could be distinguished: the proximal and distal host bone marrow, the transplanted bone graft, and the hostgraft transition zones on the proximal and distal sides. At the proximal-distal transition zone, host cells from the proximal host bone marrow were mobilized and started to invade the bone graft (Figure 2, white arrows). Structures that could potentially act as barriers to cell invasion from the host to the graft or vice versa, such as fracture fixation pins or bone fragments, did not interfere with cell migration. Rather, cells accumulated in visible clusters at such barrier sites (Figure 2). The invading cells formed a migration front, specifically from the host cell side as they penetrated the graft. Already at 3 days, the cells penetrated 200-300 µm into the bone graft (which had a total graft length of 2 mm), with some individual cells migrating even further. Strikingly, not only did host bone marrow cells invade the graft bone marrow from the proximal side, but graft cells also migrated into the distal host bone marrow in a similar fashion, but to a lesser degree (Figure 2, blue arrows). Zoom-in images highlight these distinct migration fronts from the host into the graft at the proximal transition zone (Figure 2,  $\alpha$ ) and from the graft into the host at the distal transition zone (Figure 2,  $\beta$ ). The migration events at both osteotomy sites strongly indicate a directed process with an

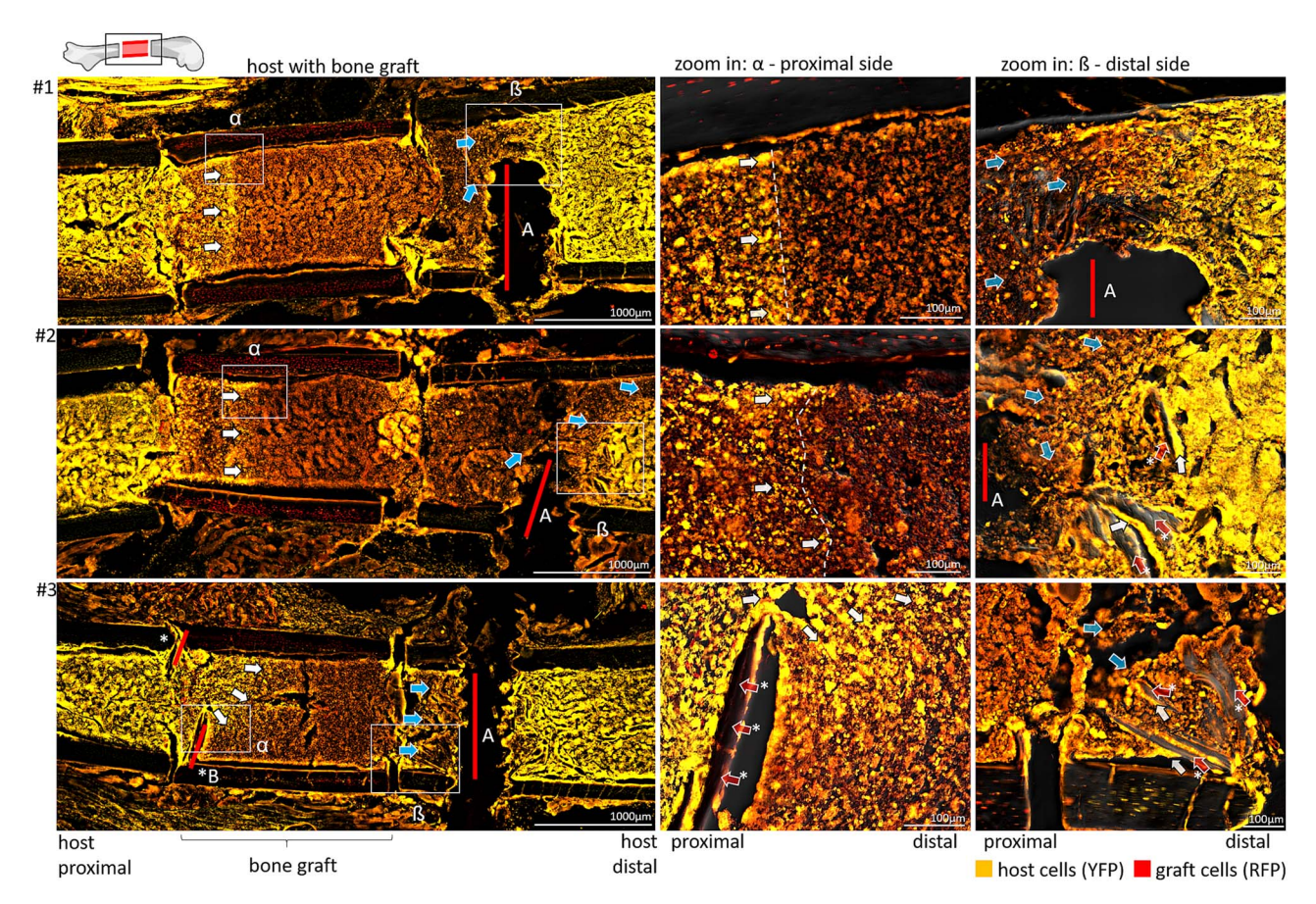


**Figure 2.** Host cells originating from the bone marrow migrated into the bone graft, progressing from the proximal to the distal region in the initial phase after transplantation. Three exemplary samples of 3 d post-transplantation. Shown are proximal host bone marrow, the transplanted bone graft and distal host bone marrow as well as the host-graft transition zones on the proximal and distal side, respectively. Yellow indicates host cells, red indicates graft cells. Host cells migrated from the proximal host bone marrow into the bone graft as indicated by white arrows. Blue arrows indicate the migration of bone graft cells into the distal host bone marrow. Red lines mark distinct barriers within the bone graft such as fixation pins (A) and bony fragments (B). White boxes indicate invasion front at the proximal and distal side for in-depth magnification.  $\alpha$  provides a zoomed-in view of the migration front on the proximal side, while  $\beta$  shows a zoomed-in view of the migration front on the distal side.

orientation from proximal to distal either from host to graft or graft to host.

# By day 7, about half of the graft bone marrow was populated with host cells, and by day 14, the bone marrow had achieved complete infiltration of host cells

At 7 d, the invasion front of host cells into the bone graft reached deep into the bone graft (Figure 3A) with about half of the graft occupied by host cells. At 14 d, the bone graft was completely invaded by host cells (Figure 3A). Graftderived cells were also detected in the outer periosteal region extending toward the adjacent soft muscle tissue, indicating outward migration of the graft cells (Figure 3A). These cells may have originated from the graft bone marrow spreading outward or may have originated from the graft periosteum itself. To further assess cell density and distribution within the bone graft at different time points, we performed nuclear staining by using SYTOX blue. Spatial distribution of cell density differed significantly from proximal to distal and this density distribution pattern changed in the graft over time (Figure 3B). At 3 d, the proximal area of the bone graft showed a decrease in cellular density compared to the host marrow and to the distal portions of the graft. At 7 d

post-transplantation, more than the proximal half of the graft showed a decreased cell density (Figure 3B). When comparing the cell density distribution in the graft to the invading host cells, a noticeable reduction in cell density ("thinning out") was observed just ahead of the advancing host cells, as indicated by the dashed white lines (Figure 3A and B). This was most prominent at the 7-d time-point, where the cell density decreased in a zone of approximately 300-400  $\mu$ m in front of the host cell invasion front (Figure 3A and B, dashed white line). At 14 d, the bone graft was uniformly re-populated by the invaded host cells (Figure 3B), indicating full infiltration of host cells into the bone graft. Evaluation of the mean intensity of nuclear cell density and its distribution across the bone graft confirmed a directional restructuring of host and graft cell distribution, with a pronounced proximal to distal organization (Figure 3C).

## Bone marrow reorganization preceded graft cell invasion, resulting in complete bone marrow reconstitution by day 14

The structured integration of the graft by host cell invasion indicates remodeling of the graft bone marrow. Movat's pentachrome staining was conducted to assess alterations in bone marrow composition, confirming substantial changes

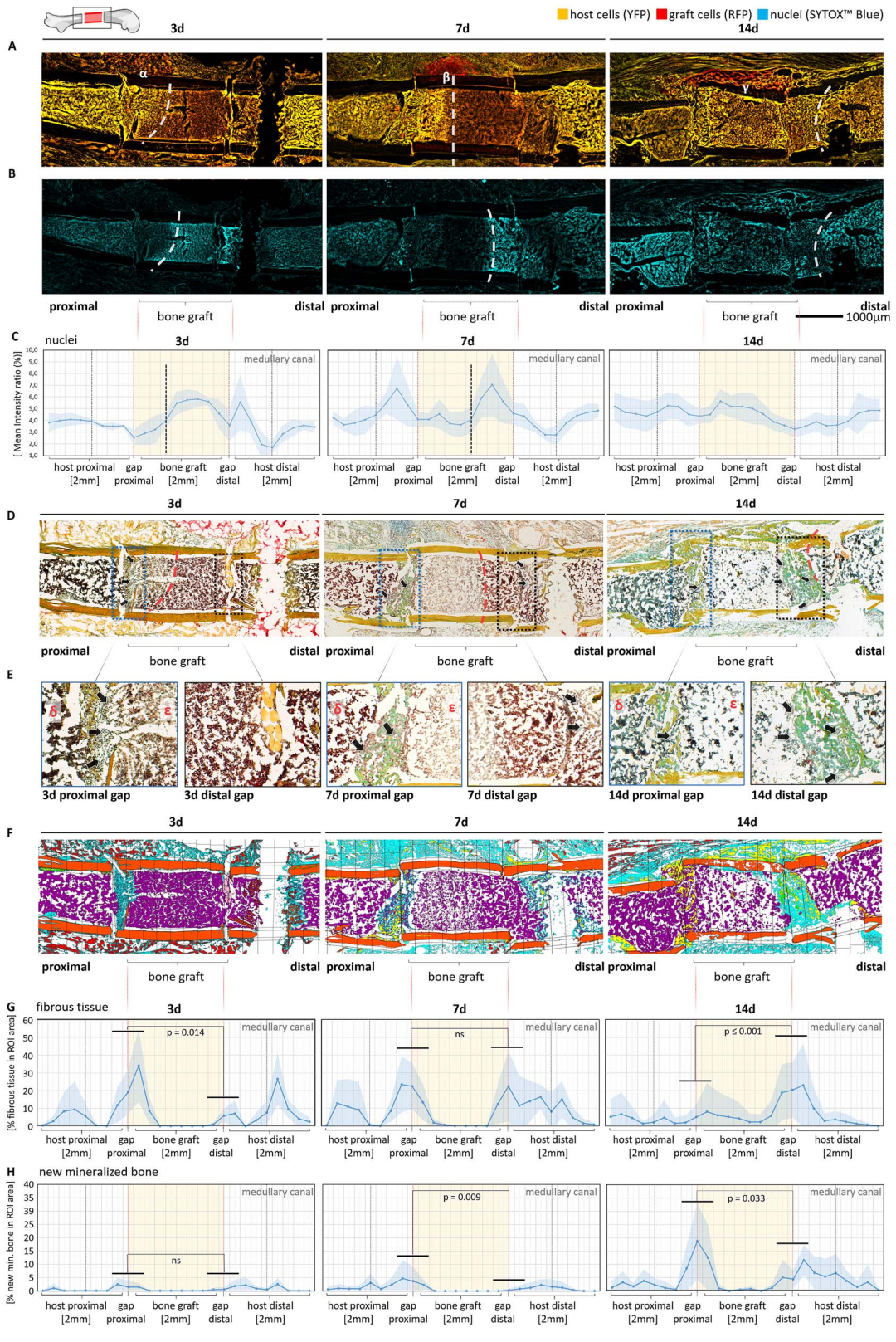


Figure 3. Fourteen days after transplantation, host cells had completely infiltrated the bone graft, with callus formation at both osteotomy sites. (A) Representative images taken 3, 7, and 14 d after transplantation. The white dashed line marks the depth of host cell invasion into the bone graft. By the 17th day, approximately half of the bone graft was infiltrated by host cells. By the 14th day, host cells completely penetrated the bone graft, reaching all the way to the distal transition zone. Notably, graft-derived cells were also detected in the outer periosteal region and adjacent soft muscle tissue, suggesting outward migration of graft cells. (B) SYTOX blue nuclei staining (cyan) shows the overall distribution and density of cells in the bone graft at different time points. The identical specimen, as shown in (A), were used for each of the different time points. Notably, significantly fewer cells were observed beyond the indicated migration front at 3 and 7 d after transplantation. In contrast, 14 d after transplantation, the cells were evenly distributed across the bone graft. (C) Mean intensity measurements of nuclear cell distribution within the bone graft confirming a directional restructuring of cell distribution from proximal to distal regions (3d (n = 5), 7d (n = 5), 14d (n = 6)). Data are presented as the mean  $\pm$  SD. (D) Movat's pentachrome staining to

of the graft bone marrow throughout the time course after transplantation (Figure 3D). At 3 d, the Movat's pentachrome staining confirmed a rather dense composition which changed toward a more loose one at 7 d of the transplanted bone marrow, matching the areas of reduced cell nuclei density (Figure 3D). By 14 d, the entire graft bone marrow exhibited a less dense composition compared to the host bone marrow (Figure 3D). This indicates that further remodeling of the graft bone marrow appears to be required for a fully restored bone marrow homeostasis. Taken together, this observation suggests that host cells not only invade the graft, but also induce changes in the graft bone marrow leading to changes in its density indicating a disassembly. This decrease in marrow density, which precedes the invading host cells, appears to be followed by proliferation of host cell populations. Subsequently, the bone marrow niche undergoes remodeling as these cells colonize the affected regions.

## Tissue composition varied in proximal versus distal host-graft transition zones across time

At both osteotomy sites (proximal and distal) significant changes in tissue formation were detected over the time course of healing (Figure 3E and F). While initially at 3 d, fibrous tissue dominated the proximal host-graft osteotomy site (21.8%), the distal one showed minimal fibrous tissue formation (4.7%) (Figure 3G, 3d). At 7 d, a marked decrease in fibrous tissue was detected proximally while fibrous tissue area significantly increased distally (Figure 3G, 7d). At 14 d, only remnants of fibrous tissue were detected proximally (5.0%) but with a further significant increase distally (20.7%) (Figure 3G, 14d). While at 3 d only minimal areas of newly formed mineralized bone tissue were detected, both proximally and distally at the osteotomies (Figure 3H, 3d), by 7 d some bone formation was detected proximally (3.6%) (Figure 3H, 7d). Finally at 14 d, significantly increased mineralized bone tissue was detected proximally compared to distally (Figure 3H, 14d). These changes in tissue composition indicate a shift from fibrous tissue to mineralized bone at both osteotomy sites as healing progresses.

## Vascular sprouts infiltrating the graft mainly emerged from the proximal host bone marrow resulting in complete vascularization of the graft by day 14

Given the critical role of angiogenesis in physiological and remodeling processes, <sup>20–23</sup> ECs were stained for CD146 to visualize and quantify the extent and directionality of microvascular assembly in the bone graft. After 3 d, vascular sprouts had emerged from the proximal side and extended to the distal side of the bone graft. Almost all microvascular

structures originated from the proximal host bone marrow and only to a lesser degree from surrounding soft tissues (Figure 4A). This is in contrast to previous analyses of angiogenesis in bone healing using single osteotomy models, where a large proportion of vascular invasion occurred from the surrounding soft tissue structures and muscles. <sup>24</sup>,25 At 7 d, the vascular sprouts penetrated deeper into the bone graft, while at 14 d, the entire bone graft was vascularized (Figure 4A). Notably, while vascular sprouting from the distal side into the graft was also observed, it was minimal and first became apparent at day 7.

Superimposing the microvascular stainings with the nuclear stainings, an area of reduced nuclear density was identified in front of the vessel invasion front (Figure 4B). The decrease in cell density in front of the microvascular invasion, compared to healthy intact bone marrow, supports the assumption that graft bone marrow remodeling is tightly linked to vascular invasion. Quantification of vascular density across the bone graft further confirmed the proximal-to-distal progression of the vascular structures (Figure 4C). A magnified image of vascular sprouts invading the graft, superimposed with nuclear staining, highlights the decrease in nuclear density in an area up to 100  $\mu$ m distal to the sprout formation front (Figure 4D). Beyond 100  $\mu$ m distal to the vascular front, however, cell density increased toward physiological levels as found in intact (host) bone marrow. Additional staining for CD31, a commonly used blood vessel marker, revealed strong co-localization with CD146-positive vascular structures (Figure 4D), while CD31 also abundantly labeled cells within the bone marrow compartment, consistent with its known expression in monocytes. 26,27 To further characterize vessel subtypes during early sprouting into the graft, we combined the endothelial markers CD31 and EMCN. This approach distinguishes arterial from venous structures, as CD31 labels both arterial and venous microvascular networks, while EMCN is restricted to venous capillaries.<sup>28</sup> Using this approach, we found that sprouts invading the graft stained for both CD31 and EMCN, showing co-localization, whereas abundant arterial structures in the surrounding muscle stained only for CD31 (Figure 4E). At 14 d, the vascular network spanned the entire bone marrow cavity of the graft. Slightly higher vascular densities were observed in the center of the medullary cavity compared to the regions immediately adjacent to the cortices (Figure S2). Overall, at 14 d, the vascular density within the graft was significantly increased compared to the host bone marrow (Figure 4C). This indicates an ongoing further remodeling of the vascular network, including vascular pruning<sup>29,30</sup> until the central arterial structure is fully restored. To better understand early regenerative events in our model, we next assessed the spatio-temporal progression of pre-osteoblasts by staining for Osterix (OSX). At 3 d,

analyze tissue compositions at 3-, 7-, and 14-d post-transplantation. Orange represents mineralized bone, yellow-green represents newly formed bone, purple represents bone marrow and turquoise represents fibroblastic cells. The blue box indicates the proximal gap, whereas the black box indicates the distal gap. Black arrows indicate fibroblastic cells in the gap,  $\delta$  indicates the proximal bone marrow,  $\varepsilon$  indicates the distal bone marrow, and the red dashed line indicates the invasion front into the bone graft. (E) Magnified images of the proximal and distal gaps at different time points showing changes in tissue composition over time at both proximal and distal sites. (F) Masked images of the samples shown in (D) used to quantify the different tissue compositions. White represents empty space, orange represents cortical bone, dark green represents cartilage, red represents muscle, purple represents bone marrow, and cyan represents fibrous tissue. (G) Percentage of fibrous tissue in the transplantation region for different groups. After 3 d, the fibrous tissue initially formed on the proximal side, but after 14 d it was predominantly visible on the distal side (3d (n = 5), 7d (n = 5), 14d (n = 6)). (H) Percentage of newly mineralized bone in the medullary canal at the different time points. The formation of mineralized bone peaked after 14 d, especially in the proximal transition zone (3d (n = 5), 7d (n = 5), 14d (n = 6)). Data are presented as the mean  $\pm$  SD. Tissue composition of the proximal and distal gaps was compared using the Mann–Whitney U test, with p < .05 considered statistically significant.

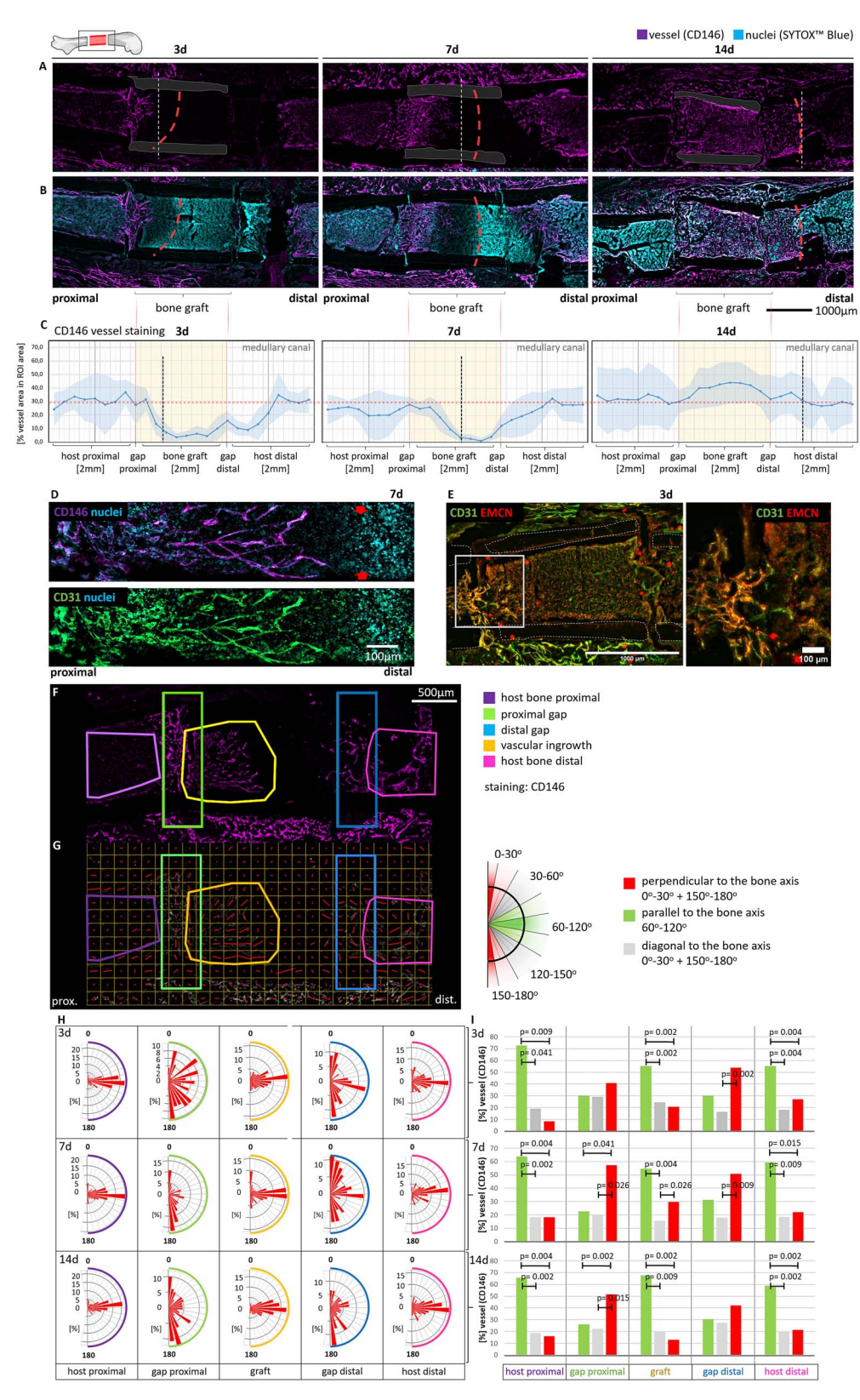


Figure 4. Vessel sprouts invading the bone graft, predominantly originating from the proximal host bone marrow, coincided with graft marrow remodeling. (A) Samples were stained for CD146 to visualize blood vessels and their infiltration into the bone graft. Vascular sprouts penetrating the bone graft were derived from the proximal bone marrow of the host. At 3 d after transplantation, only a few sprouts had infiltrated the graft, while at 7 d the proximal half of the bone graft was vascularized. After 14 d, the entire bone graft was vascularized. The cortical bone is drawn in gray on the images. (B) Images were superimposed with SYTOX nuclear staining. It appears that the cell density decreased ahead of the advancing vascular front. (C) Intensity analysis of CD146 showing the progression of sprouting angiogenesis from proximal to distal regions over the observed time period (3d (n = 5), 7d (n = 5), 14d (n = 6)). Data are presented as the mean  $\pm$  SD. (D) Zoomed-in view of vascular sprouts stained for CD146 and CD31 at 7 d, superimposed with nuclei staining. (E) Representative image from the 3-d time point stained for CD31 and EMCN. CD31- and EMCN-positive vascular sprouts were observed invading the graft, while in the surrounding muscle, arterial structures positive for CD31 were detected. (F) Blood vessel orientation based on CD146 staining. Different

OSX-expressing pre-osteoblasts emerged at the proximal host bone marrow and progressively migrated into the graft, fully repopulating it by 14 d (Figure S3A). A zoom-in image at the 7-d time point, with additional EMCN staining, confirmed the close association of OSX-expressing osteoblasts with blood vessels (Figure S3B). These findings indicate that osteoprogenitor cells migrate along blood vessels into the graft, where they contribute to initiating the healing cascade.

## Blood vessels in the host and graft bone marrow ran parallel to the bone axis, but perpendicular at the osteotomy sites

In secondary bone healing, we could show earlier that vessel structures aligned to collagen networks which counterintuitively orient perpendicular to the bone axis at the fracture site.<sup>24</sup> Given that our bone graft model partially mimics secondary bone healing as evidenced by cartilage formation at the host-graft transition zones (Figure 3D and E), we examined the extent to which it can be compared to bone healing at the osteotomy sites. Different ROIs were used to analyze vessel orientation, as shown in an example image of the 7d time point (Figure 4F). These distinct ROIs were further divided into smaller sub-ROIs. The average orientations of the blood vessels in each ROI were measured and plotted as red lines, with the line length indicating the degree of anisotropy (Figure 4G). The average orientations (from 0° to 180°) of each sub-ROI were plotted in a polar rose diagram to illustrate their distribution across all samples analyzed at 3, 7, and 14 d (Figure 4H). Indeed, while vessels in the host and graft bone marrow aligned parallel to the central bone axis, they underwent a shift in orientation perpendicular to the bone axis at both osteotomy sites (Figure 4H). Categorization of orientations as perpendicular (red, 0°-30° or 150°-180°), diagonal (gray, 30°-60° or 120°-150°), or parallel (green, 60°-120°) confirmed a significant shift perpendicular to the bone axis at the proximal gap at 7 and 14 d post-transplantation (Figure 4I). Although a noticeable trend of vessel orientation toward perpendicular directions was observed already at the 3-d time point, it did not reach statistical significance at this early stage.

## Fibrillar collagen formed primarily at host-graft interfaces, but not within the bone graft marrow

Next, we assessed the amount of fibrillar collagen. We speculated that fibrillar collagen assembly would occur at sites of de novo angiogenesis, ie, primarily starting from the proximal gap. SHG imaging was performed on samples at 3, 7, and 14 d after transplantation (Figure S4A). At the 3-d time point, SHG imaging showed clear punctate structures in the proximal gap, whereas they were almost completely absent in the distal area (Figure S4B) resulting in fibrillar collagen assembly primarily from the proximal osteotomy site. At 7 d

after surgery, collagen formation matured resulting in fibrillar structures at the proximal osteotomy and punctate structured formations beginning to occur at the distal osteotomy gap (Figure S4B). At 14 d after surgery, dense collagen fibrillar structures were visible at both osteotomy sites, proximally and distally bridging the cortical bone ends (Figure S4B) and resulting in a "closure" of the medullary cavity, similar to earlier findings observed in bone healing.<sup>24</sup> To assess the spatial alignment of vascular and fibrillar collagen structures SHG images and vessel staining were superimposed. Vascular sprouts preceded the development of fibrillar collagen in the bone marrow graft originating from proximal (Figure S5).

## Flushing the graft bone marrow resulted in distinct vessel orientations proximally

Our results suggest that bone marrow reconstitution by invading host cells and vasculature is essential for successful graft integration. Next, we aimed to understand how the absence of a bone marrow would affect invasion of host cells and assembly of vascular structures in the graft. We flushed the graft bone marrow before transplantation into the host bone and analyzed samples 14 d post-transplantation. In flushed bone marrow samples, vessels aligned parallel to the bone axis at the proximal host-graft transition zone, in sharp contrast to non-flushed bone marrow samples (Figure S6A and B). In all other areas, the orientation of the vessels remained similar between the two conditions. The orientations were further classified as perpendicular (red, 0°-30° or 150°-180°), diagonal (gray, 30°-60° or 120°-150°) or parallel (green, 60°-120°) to the central bone axis and flushed compared to nonflushed (Figure S6C). Comparison of the grouped orientations between the flushed and non-flushed grafts at 14 d posttransplantation confirmed these vascular changes in vessel orientation at the proximal host-graft interface. At the distal graft-host interface, the vessel orientation was perpendicular to the central bone axis in both conditions (Figure S6C). This suggests that the presence or absence of bone marrow, which acts as a physical barrier, determines the vascular architecture at the host-graft interface.

## Bone marrow re-established within the flushed graft through host cell population by day 14

The altered vessel orientation at the proximal gap, running parallel to the bone axis in the flushed graft compared to the non-flushed, suggests that vessels penetrate the transplant more rapidly when bone marrow is absent. Next, we thus assessed whether the bone marrow had re-established within the flushed bone graft after 14 d. No fibrillar collagen bridges formed at the proximal gap in groups with flushed bone marrow compared to the group with intact bone marrow transplantation (Figure 5A and B). Instead, fibrillar collagen was found across the whole bone graft and aligned parallel to

ROIs were used for the analysis of blood vessel orientation, which are shown in an exemplary image of the 7-d time-point (purple = proximal host bone, green = proximal gap, blue = distal gap, pink = distal host bone, yellow = proximal vascular ingrowth). (G) These distinct ROIs were further subdivided into smaller sub-ROIs. The average orientations of blood vessels in each ROI were measured and plotted as red lines, with the line length indicating the degree of anisotropy. (H) The average orientations (from  $0^{\circ}$  to  $180^{\circ}$ ) of each subROI were plotted in a polar rose diagram to illustrate their distribution across all analyzed samples at the time points of 3, 7, and 14 d. here  $180^{\circ}$  means perpendicular to the central bone axis, while  $90^{\circ}$  means parallel to the central bone axis (for 3d (n = 5), 7d (n = 5), 14d (n = 6)). (I) Orientations were further categorized as perpendicular (red,  $0^{\circ}$ - $30^{\circ}$  or  $150^{\circ}$ - $180^{\circ}$ ), diagonal (gray,  $30^{\circ}$ - $60^{\circ}$  or  $120^{\circ}$ - $150^{\circ}$ ) or parallel (green,  $60^{\circ}$ - $120^{\circ}$ ). In both the proximal and distal transition zones, the vessels shifted their orientation perpendicular to the central bone axis, while they remained parallel to the bone axis in the other areas. Kruskal–Wallis test was used, followed by Dunn's multiple comparisons post-hoc test. A p-value <.05 was considered statistically significant.

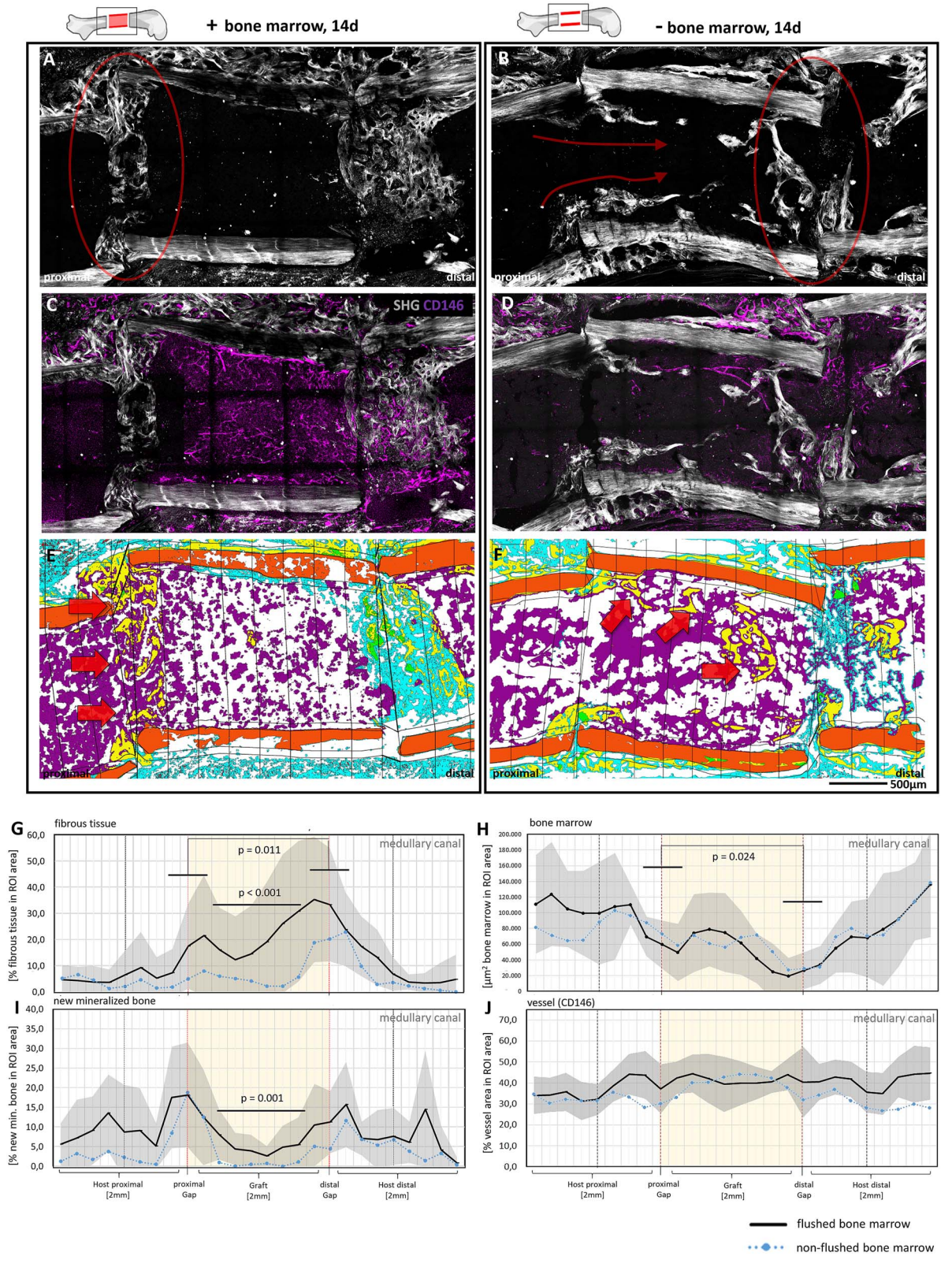


Figure 5. Bone marrow flushing from the bone graft resulted in re-establishment of the bone marrow by day 14. (A, B) At 14 d post-surgery, a comparison between the complete bone graft containing bone marrow (+bm) and a flushed graft lacking bone marrow (-bm) was conducted. SHG imaging revealed distinct differences in fibrillar collagen structures between the two groups. Notably, fibrillar collagen structures were absent at the proximal host-graft transition zone in the flushed bone graft, contrasting starkly with the bone graft containing bone marrow. Here, gray indicates fibrillar collagen, red circles highlight fibrillar collagen assembled at the transition zones, and red arrows indicate fibrillar collagen aligning and extending parallel into the bone graft. (C, D) superimposition of SHG images with vessel staining CD146. (E, F) tissue analysis was conducted utilizing Movat's Pentachrome staining. Presented here are masked images derived from the Movat's pentachrome staining. Orange represents mineralized bone, yellow represents newly formed bone, purple indicates bone marrow, and cyan indicates fibrous tissue. The red arrows highlight areas of newly mineralized bone, illustrating different distribution between the +bm and -bm samples. (G-J) the quantification of various tissue compositions in the +bm samples was compared to the -bm samples. This

the bone cortices, while collagen bridges formed at the distal osteotomy gap at 14 d (Figure 5B). We speculated that flushing the bone marrow even more enhanced invasion of host cells from the proximal side while the host bone marrow at the distal end remained as a "natural barrier" for invading cells and the successively forming collagen structures. Endothelial staining by CD146 revealed microvascular invasion in the flushed bone transplants compared to the non-flushed ones (Figure 5C and D). Movat's pentachrome staining unraveled the tissue compositions across these two conditions (Figure 5E and F). Significantly more fibrous tissue was formed at the distal host-graft interface compared to the proximal gap in the flushed group (Figure 5G). In contrast, the proximal side showed significantly greater marrow re-establishment, suggesting faster reconstitution at the proximal gap compared to the distal side (Figure 5H). Additionally, comparison of graft tissue composition between the flushed and non-flushed groups—represented in the graphs by the black and blue lines, respectively—revealed significantly greater fibrous tissue and bone formation in the flushed grafts (Figure 5G and I). While vascularization at both graft-host interfaces appeared greater in the flushed group compared with the non-flushed group (Figure 5J), detailed density analysis further revealed higher vascular density and a more compact bone marrow structure within the graft itself in the flushed condition (Figure S7). Collectively, these data suggest that new bone marrow is established faster after 14 d within the flushed graft compared to the non-flushed graft, without the need to initially degrade the existing bone marrow structure, as is necessary in nonflushed grafts.

## **Discussion**

This study introduces a novel double osteotomy bone transplantation model that enables investigation of the spatial and temporal progression of cellular migration, vascular invasion, and how this is linked to bone marrow remodeling during bone regeneration. Using fluorescent reporter mouse lines, we tracked the migration of host- and graft-derived cells. Our findings reveal a clear directional pattern of regeneration and underscore the critical role of bone marrow reconstitution: host-derived cells and CD146-positive blood vessels predominantly entered the graft from the proximal host bone marrow, coinciding with marrow remodeling and resulting in complete cellular and vascular invasion by day 14 (Figure 6).

Host cell migration and vascular invasion occurred in a coordinated, spatially organized manner, predominantly following a proximal-to-distal gradient of cellular and vascular infiltration into the graft (Figures 2-4). During regeneration, blood vessels not only deliver oxygen and nutrients to the injury site but also serve as key signaling hubs and deliver angiocrine signals and transport progenitor cells that remodel the local microenvironment.<sup>31–35</sup> The close spatial association between CD146-positive endothelial sprouts and adjacent regions of reduced graft cell density (Figure 4)

suggests that disassembly of the graft marrow is necessary to permit vascular invasion and the establishment of a de novo bone marrow niche subsequently followed by infiltration of host-derived mesenchymal progenitor cells, which contribute to niche formation. Perivascular cells associated with the invading vasculature may further support this process by secreting growth factors and cytokines known to regulate stem cell maintenance, differentiation, and niche organization.<sup>36-39</sup> Collectively, these findings indicate that invasion by proximal host-derived vascular sprouts and graft marrow remodeling are closely linked and act together to promote the establishment of a de novo bone marrow niche within the graft. The precise mechanisms underlying this remodeling, and the identity of the cell types that first migrate into the graft in association with the invading vasculature, remain to be elucidated. Future studies should also aim to clarify the mechanisms of bone marrow disassembly, eg, by assessing apoptotic markers in graft-derived marrow cells. In addition to these vascular and marrow-related changes, our analysis of tissue components at both osteotomy gap sites revealed callus formation at each graft interface, with a more pronounced response on the proximal side. Given the critical role of the periosteum in regeneration, 40,41 it is likely that periosteal cells contribute to callus formation at both osteotomy gaps. Future studies employing periosteum-specific genetic labeling or intravital time-lapse imaging could further clarify the relative contribution of periosteal cells to callus formation and bone regeneration in this model.

The graft retained resident cell populations after transplantation, indicating their transient survival before being replaced by invading host-derived vasculature and cells. In contrast, graft-derived endothelium did not survive the transplantation process. Revascularization of the graft occurred exclusively through ingrowth of host-derived blood vessels, demonstrating that graft integration relies entirely on the establishment of new vascular connections from the host rather than the persistence or adaptation of donor vasculature. This underscores the central role of host vasculature as a primary driver and regulator of the regenerative process. Our finding that vascular density within the graft exceeded that of the adjacent host marrow by day 14 likely reflects an angiogenic overshoot—a common feature of regenerative processes—aimed at rapidly meeting the metabolic demands of early tissue remodeling.<sup>29,32</sup> As regeneration progresses, this heightened vascular state is expected to resolve through pruning and regression as shown during developmental processes, 42,43 ultimately restoring microvascular homeostasis. Although the graft was fully populated with blood vessels and host cells by day 14, these findings suggest that more time is needed for complete healing and restoration to a homeostatic state.

The distinct collagen fiber alignment and blood vessel orientation observed at the invasion site after bone marrow removal from the graft—compared with non-flushed grafts—suggest that the native marrow niche plays a key

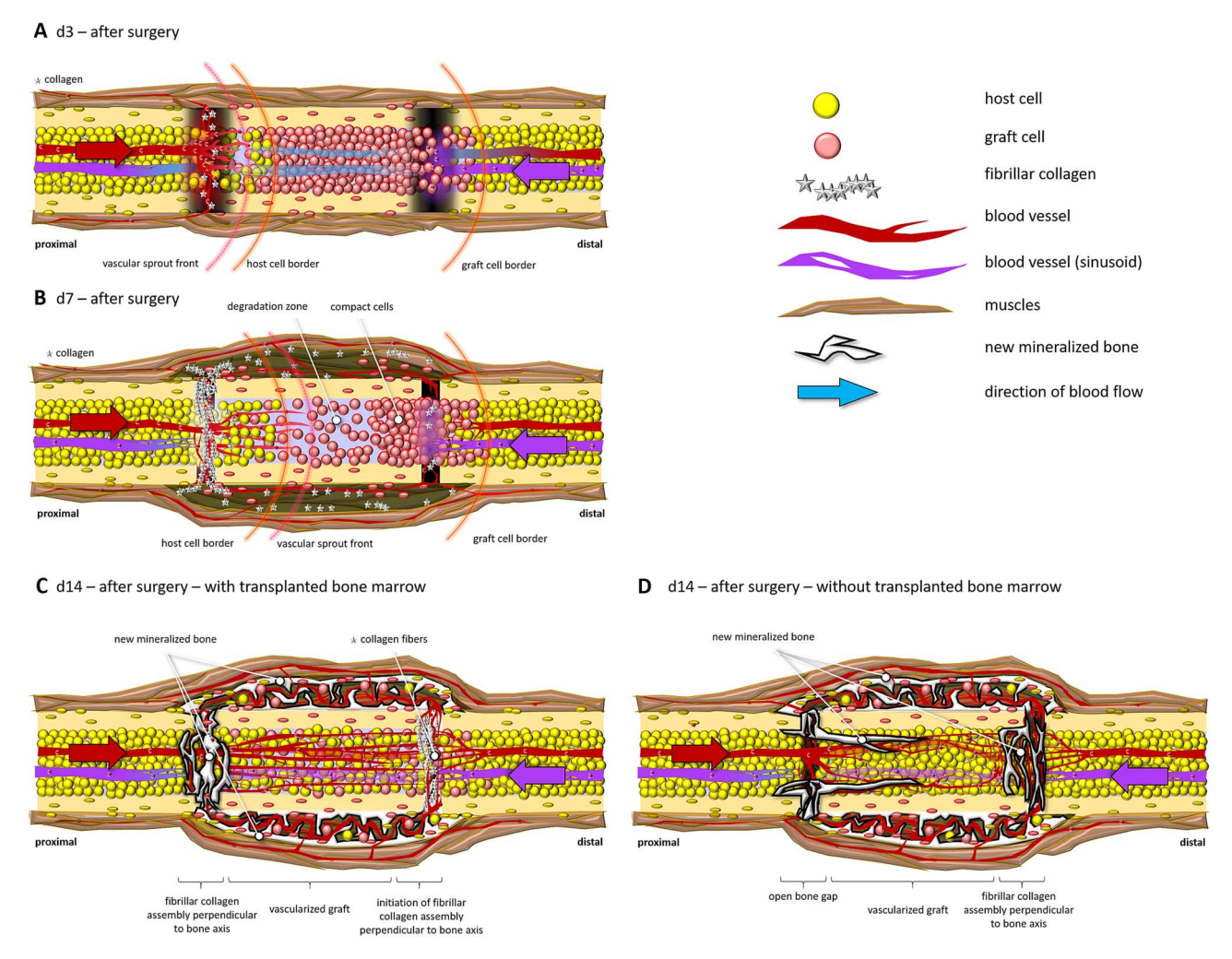


Figure 6. Illustration of the temporal progression of bone graft vascularization and bone marrow reconstitution 3, 7, and 14 d post-transplantation in bone grafts with and without flushed bone marrow. (A) At 3 d post-surgery, the transplanted graft faced reduced oxygen and nutrient supply due to blood vessel cutoff. Host cells from the proximal host bone marrow started migrating into the bone graft. Simultaneously, vessels started sprouting into the graft, progressing from the proximal to the distal side. Fibrillar collagen assembly was initiated at the proximal host-graft transition zone. (B) By day 7, approximately half of the graft was infiltrated by vessels from the proximal side. Vascular sprouts thereby preceded host cells and aligned parallel to the bone axis within the graft, while aligning perpendicular to the bone axis at the proximal gap. Graft cell migration was predominantly directed toward the distal region, where they accumulated at the distal osteotomy gap. Collagen structures organized into fibrillar fibers at the proximal gap bridging the cortical fracture ends perpendicular to the bone axis. Over time, graft bone marrow cells "thinned out" in front of the invading host cells within the graft indicating remodeling of the bone marrow at these sites. A callus like structure formed comprising the region of the transplanted bone graft. (C) At 14 d post-surgery in the +bm graft, complete vascularization occurred. Blood vessels ran perpendicular to the bone axis in the gaps and parallel to the bone axis within the graft. The bone graft was now mainly occupied by host cells, yet some graft cells persisted. In contrast, the periosteal callus primarily comprised graft cells, with only some host cells were observed. (D) In the -bm graft at 14 d, vascularization primarily occurred from the proximal to the distal gap, a pattern comparable to that seen in non-flushed bone marrow. However, at the proximal osteotomy gap they aligned parallel to the bone axis in contrast to the non-flushed graft. A significant difference was observed in the distribution of newly forming bone, which is significantly increased at the distal gap in the flushed bone marrow compared to the non-flushed samples. Some bone formation also occurred aligning and paralleling the cortices within the bone graft, which was not visible in the +bm group. The periosteal callus exhibited similarities to that observed in the +bm graft.

role in guiding the spatial organization of revascularization and tissue formation. In the absence of graft marrow, host-derived vessels appear to invade more directly, aligning along the central bone axis and facilitating rapid de novo marrow niche formation without the need for prior graft remodeling. These findings indicate that bone marrow functions not only as a source of cells but also as a physical modulator that shapes vascular patterning and the timing of vessel ingrowth. Furthermore, the more compact appearance of marrow in the flushed condition compared with the non-flushed condition suggests a faster restoration of the marrow niche, underscoring the central role of host-derived vascular and stromal populations in directing niche formation.

In summary, the here presented novel double osteotomy bone graft model offers a versatile platform to investigate the spatial and temporal dynamics of bone regeneration—particularly the coordinated progression of host cell migration and vascular invasion—and their roles in orchestrating key regenerative processes such as bone marrow remodeling. Our findings reveal a directed progression of healing cascades that are spatially and temporally coordinated, with host-derived vascular structures likely serving a central role in marrow niche reconstruction. A key strength of this model lies in its ability to track the spatial and temporal contributions of both host and graft tissues, enabling the study of bone marrow reorganization—an aspect that, to our knowledge,

has been largely overlooked in the context of its role in initiating and sustaining healing cascades. 44,45 This system also paves the way for identifying specific cell populations such as immune and other progenitor cells known to associate with the vasculature 46,47—using advanced techniques like multiplex immunofluorescence staining, thereby revealing how these cells contribute to orchestrating early regenerative events. Collectively, our findings highlight the critical role of bone marrow reconstitution and its relationship to the vasculature in bone healing and show that disassembly of the resident marrow is essential to allow invasion by extracellular matrix and microvascular structures. Notably, in transplanted bones where the marrow was flushed, reconstitution and marrow niche formation occurred to a greater extent and was accompanied by more pronounced bone formation. Future research should aim to further dissect the interactions between vascular, progenitor, and immune cells during regeneration, and to clarify how these cells contribute to early regenerative processes, with the goal of harnessing this knowledge to develop novel therapeutic strategies that enhance graft integration, vascularization, and marrow niche restoration in complex bone defects.

## **Acknowledgments**

The authors thank the DRFZ (German Rheumatism Research Center, Berlin) for providing the RFP and YFP mice. The authors also thank Gabriela Korus (Julius Wolff Institute, Berlin) for assistance with histological staining and Mario Thiele (Julius Wolff Institute, Berlin) for development of the image analysis macros.

## **Author contributions**

Julia Mehl and Tobias Thiele contributed equally to this work. Julia Mehl (Conceptualization, Formal analysis, Investigation, Visualization, Writing—original draft, Writing—review & editing), Tobias Thiele (Conceptualization, Formal analysis, Investigation, Visualization, Writing—original draft, Writing—review & editing), Agnes Ellinghaus (Methodology), Holger Gerhardt (Conceptualization, Project administration, Writing—review & editing), Georg N Duda (Conceptualization, Investigation, Project administration, Supervision, Writing—original draft, Writing—review & editing).

## Supplementary material

Supplementary material is available at IBMR Plus online.

## **Funding**

This study was funded by the German Research Foundation within the CRC1444 and DU298/26-2 and by the ERC Advanced Immuno-Mechanics.

## **Conflicts of interest**

None declared.

## **Data availability**

All data supporting the conclusions of this article are provided in the main text and supplementary material. The raw and analyzed datasets generated during this study are available from the corresponding author upon reasonable request.

### References

- Marsell R, Einhorn TA. The biology of fracture healing. *Injury*. 2011;42(6):551-555. https://doi.org/10.1016/j.injury.2011.03.031
- Bahney CS, Zondervan RL, Allison P, et al. Cellular biology of fracture healing. J Orthop Res. 2019;37(1):35-50. https://doi.org/10.1002/jor.24170
- Duda GN, Geissler S, Checa S, Tsitsilonis S, Petersen A, Schmidt-Bleek K. The decisive early phase of bone regeneration. Nat Rev Rheumatol. 2023;19:78-95. https://doi.org/10.1038/ s41584-022-00887-0
- 4. Kolar P, Schmidt-Bleek K, Schell H, et al. The early fracture hematoma and its potential role in fracture healing. *Tissue Eng Part B Rev.* 2010;16(4):427-434. https://doi.org/10.1089/ten.teb.2009.0687
- Schmidt-Bleek K, Petersen A, Dienelt A, Schwarz C, Duda GN. Initiation and early control of tissue regeneration - bone healing as a model system for tissue regeneration. *Expert Opin Biol Th*. 2014;14(2):247-259.
- Schmidt-Bleek K, Kwee BJ, Mooney DJ, Duda GN. Boon and bane of inflammation in bone tissue regeneration and its link with angiogenesis. *Tissue Eng Part B Rev.* 2015;21(4):354-364. https:// doi.org/10.1089/ten.teb.2014.0677
- Schmidt-Bleek K, Schell H, Lienau J, et al. Initial immune reaction and angiogenesis in bone healing. J Tissue Eng Regen M. 2014;8:120-130. https://doi.org/10.1002/term.1505
- Rafii S, Butler JM, Ding BS. Angiocrine functions of organspecific endothelial cells. *Nature*. 2016;529:316-325. https://doi.org/10.1038/nature17040
- Jakobsson L, Franco CA, Bentley K, et al. Endothelial cells dynamically compete for the tip cell position during angiogenic sprouting. Nat Cell Biol. 2010;12:943-953. https://doi.org/10.1038/ncb2103
- 10. Gerhardt H. Vegf and endothelial guidance in angiogenic sprouting. *Organogenesis*. 2008;4(4):241-246.
- Gerhardt H, Golding M, Fruttiger M, et al. Vegf guides angiogenic sprouting utilizing endothelial tip cell filopodia. *J Cell Biol.* 2003;161(6):1163-1177. https://doi.org/10.1083/jcb.200302047
- 12. Abdalrahman T, Checa S. On the role of mechanical signals on sprouting angiogenesis through computer modeling approaches. *Biomech Model Mechan.* 2022;21(6):1623-1640. https://doi.org/10.1007/s10237-022-01648-4
- Gebala V, Collins R, Geudens I, Phng LK, Gerhardt H. Blood flow drives lumen formation by inverse membrane blebbing during angiogenesis in vivo. *Nat Cell Biol*. 2016;18:443-450. https://doi.org/10.1038/ncb3320
- Trzpis M, McLaughlin PM, de Leij, Harmsen MC. Epithelial cell adhesion molecule: more than a carcinoma marker and adhesion molecule. *Am J Pathol*. 2007;171(2):386-395. https://doi.org/10.2353/ajpath.2007.070152
- Wang Z, Xu Q, Zhang N, Du X, Xu G, Yan X. Cd146, from a melanoma cell adhesion molecule to a signaling receptor. Signal Transduct Target Ther. 2020;5(1):148.
- 16. Shi S, Gronthos S. Perivascular niche of postnatal mesenchymal stem cells in human bone marrow and dental pulp. *J Bone Miner Res.* 2003;18(4):696-704. https://doi.org/10.1359/jbmr.2003.18.4.696
- Crisan M, Yap S, Casteilla L, et al. A perivascular origin for mesenchymal stem cells in multiple human organs. *Cell Stem Cell*. 2008;3(3):301-313. https://doi.org/10.1016/j.stem.2008.07.003
- Sweeney MD, Ayyadurai S, Zlokovic BV. Pericytes of the neurovascular unit: key functions and signaling pathways. *Nat Neurosci*. 2016;19(6):771-783. https://doi.org/10.1038/nn.4288
- Wang Z, Yan X. Cd146, a multi-functional molecule beyond adhesion. Cancer Lett. 2013;330(2):150-162. https://doi.org/10.1016/j.canlet.2012.11.049
- 20. Carmeliet P, Jain RK. Angiogenesis in cancer and other diseases. *Nature*. 2000;407:249-257. https://doi.org/10.1038/35025220
- Eelen G, Treps L, Li X, Carmeliet P. Basic and therapeutic aspects of angiogenesis updated. *Circ Res.* 2020;127(2):310-329. https://doi.org/10.1161/CIRCRESAHA.120.316851

- Kusumbe AP, Ramasamy SK, Adams RH. Coupling of angiogenesis and osteogenesis by a specific vessel subtype in bone. *Nature*. 2014;507:323-328. https://doi.org/10.1038/nature13720
- Stegen S, van Gastel, Carmeliet G. Bringing new life to damaged bone: the importance of angiogenesis in bone repair and regeneration. *Bone*. 2015;70:19-27. https://doi.org/10.1016/j.bone.2014.09.017
- Mehl J, Farahani SK, Brauer E, et al. External mechanical stability regulates hematoma vascularization in bone healing rather than endothelial yap/taz mechanotransduction. *Adv Sci (Weinh)*. 2024;11(13):e2307050. https://doi.org/10.1002/advs.202307050
- Tomlinson RE, Silva MJ. Skeletal blood flow in bone repair and maintenance. Bone Res. 2013;1:311-322. https://doi.org/10.4248/ BR201304002
- 26. Newman PJ. The biology of pecam-1. J Clin Invest. 1997;99(1):
- Metzelaar MJ, Korteweg J, Sixma JJ, Nieuwenhuis HK. Biochemical characterization of pecam-1 (cd31 antigen) on human platelets. *Thromb Haemost*. 1991;66(6):700-707. https://doi.org/10.1055/s-0038-1646488
- 28. Zhang G, Yang X, Gao R. Research progress on the structure and function of endomucin. *Animal Model Exp Med*. 2020;3(4): 325-329. https://doi.org/10.1002/ame2.12142
- Korn C, Augustin HG. Mechanisms of vessel pruning and regression. Dev Cell. 2015;34(1):5-17. https://doi.org/10.1016/j.devcel.2015.06.004
- Franco CA, Jones ML, Bernabeu MO, et al. Dynamic endothelial cell rearrangements drive developmental vessel regression. PLoS Biol. 2015;13(5):e1002125. https://doi.org/10.1371/journal.pbio.1002125
- 31. Bishop D, Schwarz Q, Wiszniak S. Endothelial-derived angiocrine factors as instructors of embryonic development. *Front Cell Dev Biol.* 2023;11:1172114.
- 32. Potente M, Gerhardt H, Carmeliet P. Basic and therapeutic aspects of angiogenesis. *Cell.* 2011;146(6):873-887. https://doi.org/10.1016/j.cell.2011.08.039
- 33. Sivan U, De Angelis, Kusumbe AP. Role of angiocrine signals in bone development, homeostasis and disease. *Open Biol.* 2019;9(10):190144. https://doi.org/10.1098/rsob.190144
- Follert P, Grosse-Segerath L, Lammert E. Blood flow-induced angiocrine signals promote organ growth and regeneration. *Bioessays*. 2025;47(2):e2400207. https://doi.org/10.1002/bies.20 2400207
- Di Maggio, Banfi A. The osteo-angiogenic signaling crosstalk for bone regeneration: harmony out of complexity. *Curr Opin Biotechnol*. 2022;76:102750. https://doi.org/10.1016/j.copbio.2022.102750

- Sivaraj KK, Adams RH. Blood vessel formation and function in bone. *Development*. 2016;143(15):2706-2715. https://doi.org/10.1242/dev.136861
- 37. Pinho S, Lacombe J, Hanoun M, et al. Pdgfralpha and cd51 mark human nestin+ sphere-forming mesenchymal stem cells capable of hematopoietic progenitor cell expansion. *J Exp Med*. 2013;210(7):1351-1367. https://doi.org/10.1084/jem.20122252
- Xu J, Wang Y, Gomez-Salazar MA, et al. Bone-forming perivascular cells: cellular heterogeneity and use for tissue repair. Stem Cells. 2021;39(11):1427-1434. https://doi.org/10.1002/ste m.3436
- 39. Tamplin OJ, Durand EM, Carr LA, et al. Hematopoietic stem cell arrival triggers dynamic remodeling of the perivascular niche. *Cell.* 2015;160(1-2):241-252. https://doi.org/10.1016/j.cell.2014.12.032
- Colnot C. Skeletal cell fate decisions within periosteum and bone marrow during bone regeneration. *J Bone Miner Res*. 2009;24(2):274-282. https://doi.org/10.1359/jbmr.081003
- 41. Ozaki A, Tsunoda M, Kinoshita S, Saura R. Role of fracture hematoma and periosteum during fracture healing in rats: interaction of fracture hematoma and the periosteum in the initial step of the healing process. *J Orthop Sci.* 2000;5(1):64-70. https://doi.org/10.1007/s007760050010
- 42. Franco CA, Jones ML, Bernabeu MO, et al. Correction: dynamic endothelial cell rearrangements drive developmental vessel regression. *PLoS Biol.* 2015;13(5):e1002163. https://doi.org/10.1371/journal.pbio.1002163
- 43. Korn C, Scholz B, Hu J, et al. Endothelial cell-derived noncanonical wnt ligands control vascular pruning in angiogenesis. *Development*. 2014;141(8):1757-1766. https://doi.org/10.1242/ dev.104422
- Lee FY, Hazan EJ, Gebhardt MC, Mankin HJ. Experimental model for allograft incorporation and allograft fracture repair. J Orthop Res. 2000;18(2):303-306. https://doi.org/10.1002/jor.1100180219
- 45. Tiyapatanaputi P, Rubery PT, Carmouche J, Schwarz EM, R JO'K, Zhang X. A novel murine segmental femoral graft model. *J Orthop Res.* 2004;22(6):1254-1260. https://doi.org/10.1016/j.orthres.2004.03.017
- Amersfoort J, Eelen G, Carmeliet P. Immunomodulation by endothelial cells - partnering up with the immune system? Nat Rev Immunol. 2022;22:576-588. https://doi.org/10.1038/ s41577-022-00694-4
- Pober JS, Sessa WC. Evolving functions of endothelial cells in inflammation. *Nat Rev Immunol*. 2007;7:803-815. https://doi.org/10.1038/nri2171